

Article

Not peer-reviewed version

Output Feedback Fuzzy Gain-Scheduling for MIMO Systems Applied to Flexible Aircraft Control

[Guilherme Chaves Barbosa](#) * and [Flávio José Silvestre](#)

Posted Date: 20 May 2025

doi: 10.20944/preprints202505.1504.v1

Keywords: Takagi-Sugeno Fuzzy; Gain-Scheduling; MIMO control; Flexible Aircraft; Output Feedback



Preprints.org is a free multidisciplinary platform providing preprint service that is dedicated to making early versions of research outputs permanently available and citable. Preprints posted at Preprints.org appear in Web of Science, Crossref, Google Scholar, Scilit, Europe PMC.

Copyright: This open access article is published under a Creative Commons CC BY 4.0 license, which permit the free download, distribution, and reuse, provided that the author and preprint are cited in any reuse.

Disclaimer/Publisher's Note: The statements, opinions, and data contained in all publications are solely those of the individual author(s) and contributor(s) and not of MDPI and/or the editor(s). MDPI and/or the editor(s) disclaim responsibility for any injury to people or property resulting from any ideas, methods, instructions, or products referred to in the content.

Article

Output Feedback Fuzzy Gain-Scheduling for MIMO Systems Applied to Flexible Aircraft Control

Guilherme C. Barbosa ^{1,*}  and Flávio J. Silvestre ^{2,†} 

¹ Research Assistant, Technische Universität Berlin

² Full Professor, Technische Universität Berlin

* Correspondence: guichavesbarbosa@gmail.com

† Current address: Marchstrasse 12, Berlin 10587, Germany.

Abstract: Previous works of our group evidenced stability problems associated with flight control law design for flexible aircraft regarding the gain-scheduling. This paper proposes an output feedback fuzzy-based gain-scheduling approach to adequate closed-loop response in a broader range of the flight envelope. This method applies a variation of the controller gains based on the membership function design for all the varying parameters, such as dynamic pressure. It aims for performance improvement while enforcing global stability gain-scheduling. The technique was demonstrated for the flexible ITA X-HALE aircraft nonlinear model and compared to the classical interpolation-based gain-scheduling technique. The results revealed that fuzzy-based gain scheduling can effectively handle high-order systems while ensuring global system stability, leading to an overall improvement in performance.

Keywords: takagi-sugeno fuzzy; gain-scheduling; MIMO control; flexible aircraft; output feedback

1. Introduction

Flight dynamics of flexible aircraft is an area that has emerged in recent years to fill the gap left by the absence of an integrated treatment of classical flight dynamics [1]. With the industry demands to reduce fuel consumption and a growing interest in the aircraft class HALE (high altitude, long endurance), the aircraft designs have become more lightweight with wings of increasing aspect ratio that increase their flexibility [2].

Most aerospace vehicles developed since 1970 have some active closed-loop control system [1]. Furthermore, the control systems development for highly flexible aircraft requires more complex models and control techniques than those adopted for slightly flexible aircraft. Classically, control law design assumes a rigid airframe accounting for steady aeroelastic effects, while dynamic aeroelastic interaction effects are only considered a posteriori, typically through gain stabilization, using low-pass and notch filters [3]. However, this procedure can lead to a low-performance controller when the flight and aeroelastic dynamics frequency ranges get closer to each other [3,4]. Several authors have addressed control law design based on flexible aircraft dynamics in the literature [3–7]. These approaches typically use structural state information as feedback signals in the control law. To keep simplicity, some of them still apply linear control theory.

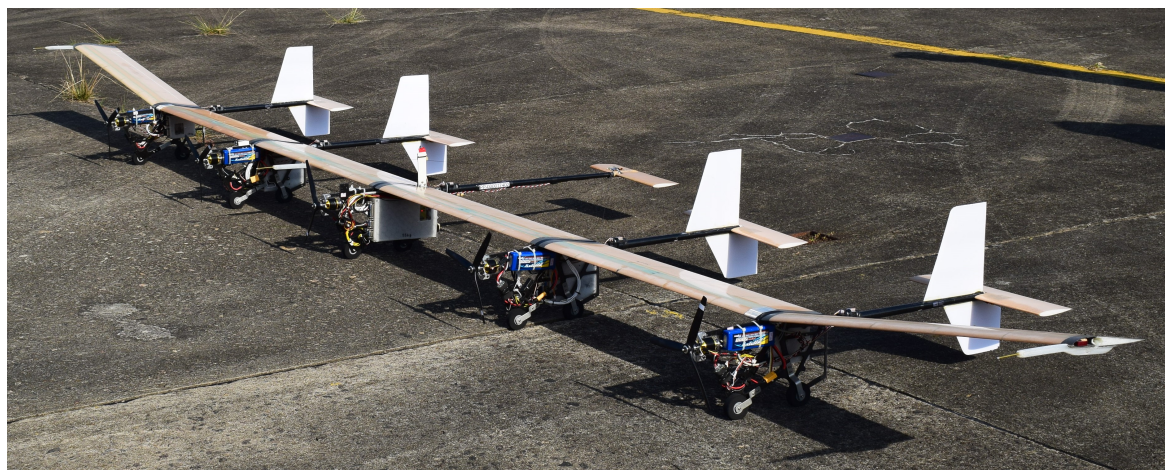


Figure 1. ITA X-HALE aircraft with six-meter wingspan that is currently in operation at ITA.

A problem in controller synthesis using linear techniques is that the linearized model represents the dynamics only in a region close to the operation point, in some cases leading to system instability when the model is subjected to significant variations, a common situation for flexible aircraft. A wide range of linear control techniques can address this issue, such as robust control, that deals with systems uncertainty [8–10]. Nonlinear techniques, such as adaptive control, can also be applied, which proposes predefined dynamics for the feedback gains that ensure stability and performance. These techniques often result in complex control laws that are hard to implement in practice [11,12].

Gain-scheduling is the predominant method used in industry to develop a full-envelope flight control law [13]. For fixed-structure, linear-model-based controllers, gain-scheduling is a good strategy since it continuously varies the controller coefficients, calculated for various operation points in the envelope, according to the current flight condition [14]. However, classical gain-scheduling can cause abrupt changes in gains, which directly affect the dynamics of the model, and may generate an undesirable performance [15]. On the other side, previous fuzzy logic applications to gain-scheduling in flight control demonstrated the feasibility of this approach [15–18]. The fuzzy membership functions provide the control parameters interpolation in a fuzzy-logic-based method that allows an adjustment for a smoother controller gains variation. Another advantage over classical gain-scheduling is that closed-loop stability can be analytically guaranteed [19].

In this context, this paper proposes to investigate the gain-scheduling effectiveness via interpolation between design points, taking advantage of the fuzzy gain-scheduling characteristic that allows a global stability analysis. Based on this characteristic, a method that combines performance and stability is proposed and evaluated. A similar method was first proposed for state feedback [20], and in this paper, it is extended to output feedback.

To carry out this investigation, the X-HALE (Experimental High-Altitude Long-Endurance) aircraft was used. This aircraft was conceived to be the University of Michigan (U-M) testbed, to provide in-flight data to validate formulations for very flexible aircraft flight dynamics [2]. Flight tests of the X-HALE have been carried out at U-M since the early 2010s. Jones and Cesnik [21] presented preliminary data obtained from the initial flight tests of a lightly instrumented X-HALE version. Furthermore, they conducted a comparative analysis between the flight test data and numerical results obtained using the U-M Nonlinear Aeroelastic Simulation Toolbox (UM/NAST). Unfortunately, due to the limited instrumentation available on the vehicle at that time, it was not possible to establish definitive correlations between theory and experimentation.

In 2014, the University of Michigan (U-M) and the Aeronautics Institute of Technology (ITA) in São José dos Campos, Brazil, formed an agreement, allowing ITA to build and test the X-HALE aircraft. While both U-M and ITA X-HALEs share a common airframe design, encompassing wing, boom, and tail, along with similar materials, airfoils, and dimensions, they exhibit notable distinctions in

their electric, electronic, flight control, instrumentation, and propulsion systems. Flight tests of the four-meter-span ITA X-HALE-4 commenced in July 2017, offering insights into the complexities of flexible aircraft flight testing. Notably, this configuration intentionally lacks a rudder and has degraded lateral-directional handling qualities. In October 2019, flight tests of the six-meter-span ITA X-HALE-6 began, equipped with additional sensors, including strain gauges at four wing stations for bending and torsion strain measurement, and two extra all-moving horizontal tails, shown in Figure 1. As of the time of writing this paper, the ITA X-HALE-4 has flown 48 times, while the ITA X-HALE-6 has flown 4 times [22].

The proposed method is demonstrated for the flexible aircraft ITA X-HALE six-meter-span nonlinear model to schedule its stability augmentation system (SAS) gains and compared to the linear-interpolation-scheduling approach. The model used disregards the white vertical fins of the tail, which appear in the version shown in Figure 1. The results revealed that the approximation introduced in the section 2.4 enables the resolution of the LMI for higher-order systems (with 36 states) and that the methodology can guarantee and enhance the stability margins of the controller, as shown in the section 4.1.

This paper is organized as follows: Section II contains the theoretical development of the proposed controller design method, which includes an explanation of the fuzzy-logic-based gain-scheduling, a proof of global stability, and the methodology for combining performance and stability. In Section III, the numerical model and the performed order model reduction are briefly described. Section IV presents the application of the methodology to the ITA X-HALE model, along with simulation results. Finally, the most important conclusions are presented in Section V.

2. Theoretical development

2.1. Linear Control Law Design

Flexible aircraft may exhibit undesirable flight dynamics characteristics stemming from various factors. In such instances, a viable recourse entails the implementation of a SAS aimed at enhancing stability margins and adjusting the aircraft's behavior according to desired patterns.

To enhance stability and obtain an adequately damped response, a proportional output-feedback controller (block K in Figure 2) is usually used in the inner-loop. A way to design the SAS gains is using the Linear Quadratic Regulator (LQR) technique. First, the model is linearized, achieving the state-space system:

$$\begin{aligned}\dot{x} &= Ax + Bu \\ y &= Cx\end{aligned}\tag{1}$$

where $x \in \mathbb{R}^n$ is the state vector, $u \in \mathbb{R}^m$ is the control input and $y \in \mathbb{R}^p$ is the measured output [23]. The SAS control signal is the output feedback given by:

$$u_{SAS} = Ky\tag{2}$$

which leads to a closed loop given by:

$$\dot{x} = (A + BKC)x = A_c x.\tag{3}$$

The LQR formulation allows to calculate the feedback gain matrix K by minimizing the performance index (PI) J , a cost function defined as:

$$J = \frac{1}{2} \int_0^\infty (x^T Q x + u^T R u) dt\tag{4}$$

where R is a positive definite control weighting matrix and Q is a positive semidefinite state weighting matrix. The PI in the LQR problem can be calculated with the matrix P obtained from the solution of the Lyapunov equation:

$$0 = A_c^T P + P A_c + Q - C^T K^T R K C \quad (5)$$

A gain matrix that minimizes the PI is desired. If the closed-loop system is asymptotically stable, the PI can be calculated with the equation:

$$J = \frac{1}{2} x^T(0) P x(0) = \frac{1}{2} \text{tr}(P x(0) x^T(0)) \quad (6)$$

If the model is open-loop unstable, an initial stabilizing gain is calculated by minimizing the maximum real part of the eigenvalues of A_c . Then Eq. (5) is solved numerically in an iterative process to minimize J in Eq. (6) [23].

2.2. The Gain-Scheduling Problem

Linearized models cannot represent the entire flight envelope due to significant changes in the dynamic pressure during operation, which considerably modify the rigid body and aeroelastic dynamics. As a result, a constant linear model cannot be used to describe the entire flight envelope, and traditional methods with a fixed gain set cannot fulfill the design requirements [14]. Gain-scheduling, whose principle is adjusting the control law with the change of scheduling variable, is a control technique that enables the control parameters interpolation between different design points to accomplish satisfactory control tasks.

2.2.1. Classical Gain-Scheduling

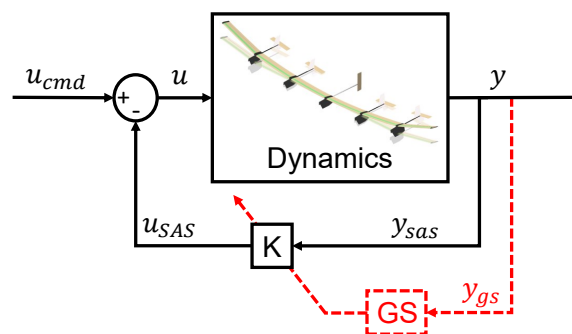


Figure 2. Flight control system block diagram

A gain-scheduled controller design for a nonlinear model can be described as a four-step procedure. The first step is to compute a linearization of the nonlinear model in the desired equilibrium points, also called operating points or set points. The second step uses linear design methods to design linear controllers for each linear model obtained in the previous step to achieve the requirements for each equilibrium condition. The third step consists in implementing the linear controllers family such that the controller coefficients (gains) are varied (scheduled) according to the current value of the scheduled variables [14], represented in Figure 2 by “GS”. Finally, the fourth step is performance and stability evaluation. Typically, stability can be assured only locally and in a slow-variation setting, but it is by far not guaranteed. The same applies to control performance. Depending on the scheduling strategy, performance may fall drastically [15]. Normally, stability and performance must be assessed based on simulation studies [14]. Depending on the number of parameters that may vary and change the model, the number of simulations to be performed may increase drastically, resulting in a very costly control law development process.

2.2.2. Fuzzy-logic-based Gain-Scheduling (FGS)

The fuzzy logic is based on “IF antecedent THEN consequence” rules, and any rule is composed by an antecedent and a consequence, where both can receive more than one preposition. Among the fuzzy logic classes, the Takagi-Sugeno (TS) one has the particularity of containing a linear input-output relation in the consequence [24].

The FGS controller that we propose in this paper is a TS-type fuzzy controller and follows the same steps as the classical gain-scheduling. However, it employs a different interpolation strategy, which enables a stability analysis of the fuzzy model [19].

At each design point y_{gs_i} ($i = 1, 2, \dots, l$), with l design variable points, the system described in Eq. (1) is approximated by the fuzzy rule as follows below:

$$R_i : \text{ If } y \text{ is } y_{gs_i} \text{ then } \dot{x} = A_i x + B_i u \text{ and } y = C_i x \quad (7)$$

where R_i is the i^{th} rule, y_{gs_i} is the fuzzy set for each rule, “ y is y_{gs_i} ” is the antecedent (given that y is the scheduled variable crisp value) and “ $\dot{x} = A_i x + B_i u$ and $y = C_i x$ ” is the consequence, with two linear input-output relations. The control law is defined by:

$$R_i : \text{ If } y \text{ is } y_{gs_i} \text{ then } u = K_i y \quad (8)$$

The membership functions used to interpolate the rules can have many forms (triangular, trapezoidal, bell, Gaussian, etc). The Gaussian form was selected in this work because it ensures a smooth transition between gains while emphasizing the influence of the closest design point. The corresponding weights are given by:

$$\mu_i(v) = \exp\left(-\left(\frac{y - y_{gs_i}}{2\sigma}\right)^2\right) \quad (9)$$

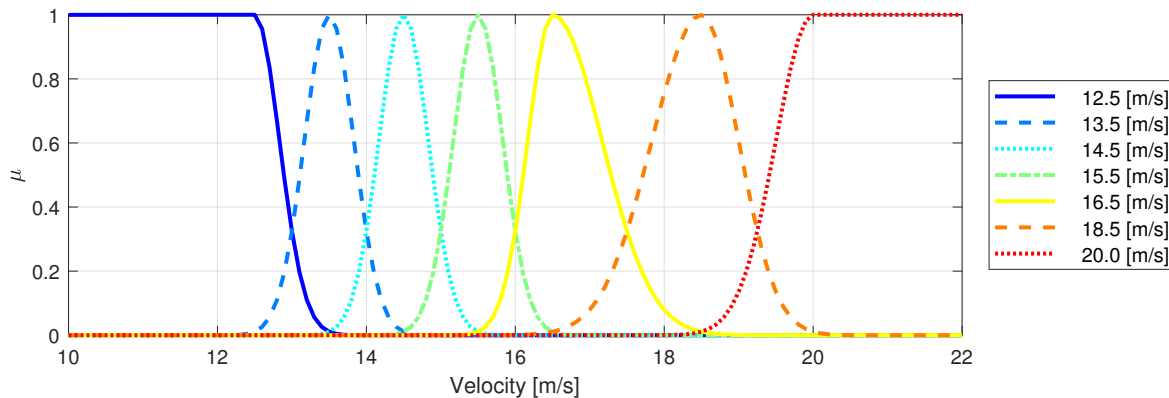


Figure 3. Designed membership functions

The weight is the mathematical form to ponder each rule according to the scheduled variable value, and σ (standard deviation) is a design parameter that measures how the neighbor antecedents affect the consequence. If σ is too small, the controller's transition becomes excessively sharp. Conversely, if σ is too large, the influence of nearby design points may exceed the desired level. We selected a set of σ values such that, at the design point, the weight of the nearest neighbors approaches zero, while at the midpoint, both points are assigned equal weight. In Figure 3, seven membership functions (μ), one for each velocity selected, with Gaussian form, are displayed, and the weight for each rule is given by μ . Eventually, the weights are normalized by the sum of all rules weights so that the sum of all normalized weights is always equal to 1. Therefore, the normalized weights ω_i are given by:

$$\omega_i = \frac{\mu_i}{\sum_{i=1}^l \mu_i} \quad (10)$$

The system can now be represented by:

$$\dot{\mathbf{x}} = \sum_{i=1}^l \omega_i (\mathbf{A}_i \mathbf{x} + \mathbf{B}_i \mathbf{u}), \quad (11)$$

$$\mathbf{y} = \sum_{i=1}^l \omega_i (\mathbf{C}_i \mathbf{x}), \quad (12)$$

and the control law by:

$$\mathbf{u} = \sum_{i=1}^l \omega_i (\mathbf{K}_i \mathbf{y}). \quad (13)$$

The FGS controller effectiveness relies on tuning both the LQR controllers and σ . The LQR parameter affects the performance and stability at each design point (one LQR design for each fuzzy rule), and σ tunes how smooth the transition between these points will be.

2.3. Fuzzy Gain-Scheduling Design Taking Into Account Global Stability

The closed-loop stability assessment is based on the Lyapunov direct method. The Lyapunov direct method seeks to determine the Lyapunov function parameters belonging to a particular candidate class that guarantees the stability of the investigated system [25]. This analysis will be conducted starting from a Lyapunov candidate in the quadratic form

$$V = \mathbf{x}^T \mathbf{P} \mathbf{x} \quad (14)$$

and then proceeding according to the second Lyapunov method [26].

Therefore, the parameterization occurs in the search for a single symmetric positive definite matrix \mathbf{P} , which simultaneously satisfies a constraint set in the form of linear matrix inequalities (LMI). For the open-loop system described in Eq. 11, the time derivative of the Lyapunov candidate function will be

$$\dot{V} = \dot{\mathbf{x}}^T \mathbf{P} \mathbf{x} + \mathbf{x}^T \mathbf{P} \dot{\mathbf{x}} \quad (15)$$

$$= \mathbf{x}^T \mathbf{A}(\omega)^T \mathbf{P} \mathbf{x} + \mathbf{x}^T \mathbf{P} \mathbf{A}(\omega) \mathbf{x} \quad (16)$$

$$= \mathbf{x}^T [\mathbf{A}(\omega)^T \mathbf{P} + \mathbf{P} \mathbf{A}(\omega)] \mathbf{x} \quad (17)$$

$$= \mathbf{x}^T \sum_{i=1}^l \omega_i [\mathbf{A}_i^T \mathbf{P} + \mathbf{P} \mathbf{A}_i] \mathbf{x} \quad (18)$$

where $\mathbf{A}(\omega)$ is the final value of all the fuzzy rules, $\mathbf{A}(\omega) = \sum_{i=1}^l \omega_i \mathbf{A}_i$. This notation will also find application in subsequent matrices.

Since the $\sum_{i=1}^l \omega_i$ is always equal to one, see Eq. 10, rather than satisfying Eq. 18, it would suffice to satisfy the Theorem presented below, which involves a set of coupled Lyapunov inequalities, to ensure stability in the Lyapunov sense.

Theorem 1. [25]. *The system represented in Eq. 11 is asymptotically stable if there is a symmetric positive definite matrix \mathbf{P} that satisfies*

$$\mathbf{A}_i^T \mathbf{P} + \mathbf{P} \mathbf{A}_i < 0, i = 1, 2, \dots, l. \quad (19)$$

In order to calculate the controller gains, first for a state feedback, they will be inserted into the derivative of the Lyapunov function in Eq. 16 for the closed-loop case, resulting in:

$$\dot{V} = \mathbf{x}^T [\mathbf{A}(\omega) + \mathbf{B}(\omega) \mathbf{K}(\omega)]^T \mathbf{P} \mathbf{x} + \mathbf{x}^T \mathbf{P} [\mathbf{A}(\omega) + \mathbf{B}(\omega) \mathbf{K}(\omega)] \mathbf{x} \quad (20)$$

$$= \mathbf{x}^T ([\mathbf{A}(\omega) + \mathbf{B}(\omega) \mathbf{K}(\omega)]^T \mathbf{P} + \mathbf{P} [\mathbf{A}(\omega) + \mathbf{B}(\omega) \mathbf{K}(\omega)]) \mathbf{x}. \quad (21)$$

Therefore, it is enough to ensure

$$[A(\omega) + B(\omega)K(\omega)]^T P + P[A(\omega) + B(\omega)K(\omega)] < 0. \quad (22)$$

At this point, it is noted that the inequality is not an LMI since there are two matrix variable sets to be determined that are multiplied: one being the matrix $K(\omega)$ and the other being the matrix P . The simplicity by which such inequalities can be converted into LMI is the great attraction of quadratic stability. Using the transformations $W = P^{-1}$ and $Z(\omega) = K(\omega)W$ the equivalent condition is obtained:

$$Z(\omega)^T B(\omega)^T + W A(\omega)^T + A(\omega)W + B(\omega)Z(\omega) < 0 \quad (23)$$

$$\sum_{i=1}^l \sum_{j=1}^l \omega_i \omega_j (Z_j^T B_i^T + W A_i^T + A_i W + B_i Z_j) < 0 \quad (24)$$

Thus the following Theorem was achieved, given that a linear set of inequalities in the W and Z_i variables is now available.

Theorem 2. [25]. *The system represented in Eq. 11 is asymptotically stable if there is a symmetric positive definite matrix W and any matrices Z_i that satisfy*

$$\begin{aligned} W A_i^T + A_i W + Z_i^T B_i^T + B_i Z_i &< 0, i = j = 1, 2, \dots, l. \\ W A_i^T + A_i W + W A_j^T + A_j W + Z_j^T B_i^T + B_i Z_j + Z_i^T B_j^T + B_j Z_i &< 0, i < j, i = j = 1, 2, \dots, l. \end{aligned} \quad (25)$$

Suppose that there is a feasible solution to the inequalities presented in Theorem 2. In that case, the stabilizing controller gains can be obtained by solving $K_i = Z_i W^{-1}$, and also the Lyapunov function that guarantees stability to the closed-loop system for these projected gains, obtained from the inverse of W .

However, there are situations where the state feedback controller is restricted since it would be necessary to use state observers for a large number of states. That is the case of flexible aircraft dynamic models, which usually have a high-order model. Thus, we adapt the method for the output feedback case in the following section.

2.4. Fuzzy Gain-Scheduling with Output Feedback

Considering the feedback of only the measured outputs, given by the output matrix C , the Lyapunov candidate in Eq. 21 is expanded as:

$$W[A(\omega) + B(\omega)K(\omega)C(\omega)]^T + [A(\omega) + B(\omega)K(\omega)C(\omega)]W < 0. \quad (26)$$

$$A(\omega)W + W A(\omega)^T + B(\omega)K(\omega)C(\omega)W + W C(\omega)^T K(\omega)^T B(\omega)^T < 0. \quad (27)$$

The stability condition is no longer a set of LMI since both $K(\omega)$ and W are variables. A similar problem was faced in the previous section. The solution is also similar, transforming the variables until a set of LMI was achieved. To transform these inequalities to LMI, two transformations are necessary [27], the first being $MC = CW$, where C must be full row rank, resulting in:

$$A(\omega)W + W A(\omega)^T + B(\omega)K(\omega)M(\omega)C(\omega) + C(\omega)^T M(\omega)^T K(\omega)^T B(\omega)^T < 0, \quad (28)$$

and the second $K = NM^{-1}$, resulting in the following LMI:

$$A(\omega)W + W A(\omega)^T + B(\omega)N(\omega)C(\omega) + C(\omega)^T N(\omega)^T B(\omega)^T < 0. \quad (29)$$

However, these transformations include an equality relation $MC = CW$. In order to keep the LMI set as simple as possible, once the system already has high order and complexity, that equality was converted into an approximate LMI.

$$M(\omega)C(\omega) = C(\omega)W, \quad (30)$$

$$M(\omega)C(\omega) - C(\omega)W = 0. \quad (31)$$

This equality can be approximated by:

$$\begin{bmatrix} -\kappa I & [M(\omega)C(\omega) - C(\omega)W]^T \\ [M(\omega)C(\omega) - C(\omega)W] & -I \end{bmatrix} < 0. \quad (32)$$

The left-hand-side matrix in the LMI is Hermitian or real symmetric matrix, and the inequality aims to ensure that it is negative definite, which makes this approximation valid. This occurs because, under these conditions, the matrix has two key properties [28]:

- all diagonal elements must be less than 0, that implies $\kappa > 0$;
- the matrix must be diagonally dominant, in other words, the matrix largest magnitude value elements must be at the main diagonal.

The second property delineated above underscores the dependency of the approximation of Eq. 31 on the variable κ . Consequently, the overarching objective is to achieve a small positive value for κ , ensuring the convergence of the right-hand side of Eq. 31 towards zero. It is, nevertheless, imperative to strike a judicious balance to prevent κ from diminishing to an extent that might render the LMI infeasible. With the approximation proposed, the following LMI sets were obtained:

$$\begin{aligned} A_i W + W A_i^T + B_i N_i C + C^T N_i^T B_i^T &< 0, i = j = 1, 2, \dots, l; \\ W A_i^T + A_i W + W A_j^T + A_j W + C^T N_j^T B_i^T + B_i N_j C + \\ C^T N_i^T B_j^T + B_j N_i C &< 0, i < j, i = j = 1, 2, \dots, l; \end{aligned} \quad (33)$$

$$\begin{bmatrix} -\kappa I & [MC - CW]^T \\ [MC - CW] & -I \end{bmatrix} < 0.$$

Solving the LMI set, the gains can be recovered using the relation $K_i = N_i M^{-1}$, where N_i and M are accessed directly from LMI resolution. Note also that a constant C matrix is assumed for all design points in this formulation, which reduces the number of LMI to be solved. In cases where the output matrices vary across different design points, the formulation can still be applied. However, in such cases, an approximation, as represented in Eq. 32, must be employed for each distinct output matrix, as there will be l equations of the form $M_i C_i = C_i W$.

Therefore, the LMI set, Eq. 33, enables a design that guarantees the global asymptotic stability for a nonlinear system described according to Eqs. 11 to 13.

2.5. A new FGS Methodology Combining Stability and Performance

Despite the global stability, the method discussed so far does not introduce any performance requirement. The resulting gains may present an inadequate response. In this sense, studies [29,30] have been carried out to insert performance criteria in the solution of these equations, unfortunately resulting in a considerable increase in the computational cost of the method. We propose here an efficient way of including a performance specification in the solution.

Combining the set of LMI shown in Eq. 33, and a focus on performance improvement through LQR, a methodology for designing a fuzzy gain-scheduling controller is proposed following the steps shown in the flowchart in Figure 4:

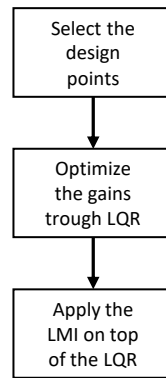


Figure 4. Flowchart of the optimization process of FGS.

1. the initial step involves selecting a set of state-space representations of the system to ensure an effective representation of the original system;
2. subsequently, the second step entails the minimization of the PI for each design point;
3. the concluding step involves the computation of stabilizing gains utilizing LMI (Eq. 33). In this phase, the system is considered in closed-loop configuration, incorporating gains determined in the preceding step. An additional gain is then calculated to ensure global asymptotic stability of the system.

The resulting gain matrix can be expressed as follows:

$$K = K_{LQR} + K_{LMI} \quad (34)$$

In this approach, the delta gains obtained from the LMI formulation represent adjustments to the nominal controller parameters. Small delta gains imply that the adapted controller closely approximates the behavior of the optimal controller derived from the LQR design, thereby minimizing performance degradation. However, it is important to emphasize that, while the LMI framework ensures global stability of the closed-loop system, it does not inherently guarantee that the delta gains will be small. Consequently, a trade-off emerges: although global stability is achieved through the LMI solution, this may come at the cost of a deviation from the optimal LQR parameters.

3. ITA X-HALE Model

3.1. Model Description

The mathematical formulation used to model the ITA X-HALE flight dynamics is based on the equations of motion derived for dually-constrained axes [31,32]. In this formulation, the origin S of the structural axes, corresponding to a material point without elastic displacement, can be non-coincident with the origin O of the body axes used in the equations of motion. In calculating equilibrium conditions, all the structural degrees of freedom are considered. In modeling the nonlinear flight dynamics around equilibrium, a reduced set of inertia-relieved constrained modes of vibration [31,32] are retained.

The aerodynamic model of the aircraft is based both on the doublet-lattice method [33] and on the vortex-lattice method [34] to which the former reduces at zero frequency. Rational function approximations [31,35] make the representation of aerodynamic loads possible in the time domain. Consequently, a significant number of aerodynamic lag states arise to make the approximation sufficiently accurate. The induced drag is also modeled based on the method of Ref. [36].

The wing structural-dynamic model consists of beam finite elements along the span. Beam elements are also used for the connection between the wing and the booms and for the booms themselves. The horizontal tails are modeled with rigid elements. Small deformations are assumed.

For control system design purposes, linear-time-invariant realizations of the nonlinear model under small disturbances around different equilibrium flight conditions are considered for the six-meter-span aircraft with a vertical central tail. The system of linear equations is then given by:

$$\dot{\mathbf{x}} = \mathbf{A}\mathbf{x} + \mathbf{B}\mathbf{u}_{ctrl} \quad (35)$$

$$\mathbf{y} = \mathbf{C}\mathbf{x} + \mathbf{D}\mathbf{u}_{ctrl} \quad (36)$$

where $\mathbf{A} \in \mathbb{R}^{n \times n}$ is the state matrix, $\mathbf{B} \in \mathbb{R}^{n \times m}$ is the control matrix, $\mathbf{C} \in \mathbb{R}^{p \times n}$ is the output matrix and $\mathbf{D} \in \mathbb{R}^{p \times m}$ is the direct-feed matrix.

The vector of disturbances of the state variables around the equilibrium conditions is given by:

$$\mathbf{x} = [V \ \alpha \ q \ \theta \ H \ x \ \beta \ \phi \ p \ r \ \psi \ y \ \lambda_{rb}^T \ \boldsymbol{\eta}^T \ \dot{\boldsymbol{\eta}}^T \ \lambda_{\eta}^T]^T \quad (37)$$

where $\mathbf{x} \in \mathbb{R}^{n \times 1}$ and disturbances with respect to the equilibrium states are implicit.

The model includes the kinematic equations in the inertial reference frame for all six rigid-body degrees of freedom: displacements in the x and y directions, altitude H , and roll, pitch, and yaw angles (ϕ , θ and ψ , respectively). Furthermore, the velocity V , the angle of attack α , the sideslip angle β , as well as the angular rates p , q , and r also have their corresponding equations of motion. The structural dynamics are represented by modal coordinates. The modal amplitudes and their time derivatives are given by $\boldsymbol{\eta}$ and $\dot{\boldsymbol{\eta}}$, respectively. Modes of vibration with frequencies up to 25 Hz are retained in the model. Aerodynamic lag states due to rigid-body and control-surface dynamics (λ_{rb}) and due to the aeroelastic dynamics (λ_{η}) are also included. [Guimarães Neto et al. \[22\]](#) make a more in-depth description of the model and also present a validation of the numerical results with flight test data.

Moreover, actuation system elements make up the control inputs of the aircraft: the elevons, the ailerons, and the electric motors, all of which can be independently controlled. Figure 5 shows the corresponding nomenclature of each control input for the six-meter-span ITA X-HALE aircraft.

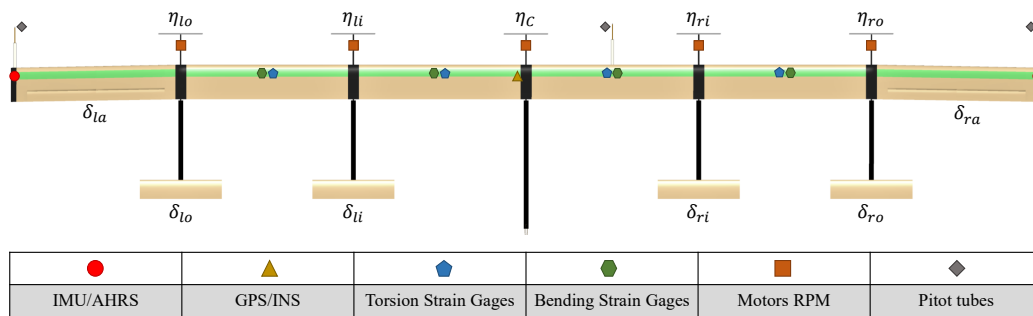


Figure 5. Six-meter-span ITA X-HALE configuration and the control inputs and sensors description.

Therefore, for the six-meter-span ITA X-HALE, the linear model comprises $n = 352$ states: 12 from rigid-body motion; 83 from rigid-body and control-surface aerodynamic lag states; 58 from elastic states; and 199 from aeroelastic aerodynamic lag states. Also, the model presents a total of $m = 11$ control input variables, whose disturbances around the equilibrium flight conditions are given by:

$$\mathbf{u}_{ctrl} = [\delta_{li} \ \delta_{ri} \ \delta_{lo} \ \delta_{ro} \ \delta_{la} \ \delta_{ra} \ \eta_{lo} \ \eta_{li} \ \eta_c \ \eta_{ri} \ \eta_{ro}]^T \quad (38)$$

where $\mathbf{u}_{ctrl} \in \mathbb{R}^{m \times 1}$. The variables corresponding to the control surface deflections are given in degrees, whereas the ones corresponding to the throttle setting of each motor vary from zero to one (full throttle).

All aircraft actuators (Eq. (38)) can be independently commanded. However, a couple of command rules mixing the actuators are enforced to reduce the number of gains to be determined once we can assume that the aircraft is nearly symmetric with respect to the xz plane. In this mixing, it was defined

that the inner elevons δ_{li} and δ_{ri} operate symmetrically as elevators ($\delta_{li} = \delta_{ri}$) and the outer elevons δ_{lo} and δ_{ro} operate anti-symmetrically ($\delta_{li} = -\delta_{ri}$). The outer electric motors are used differentially to generate yawing motion ($\eta_C - (\eta_{lo} + \eta_{li}) = (\eta_{ro} + \eta_{ri}) - \eta_C$), in substitution of a rudder, while all motors operate together to generate thrust - in this case, the total thrust is due to the sum of all motors ($\eta_C + \eta_{lo} + \eta_{li} + \eta_{ro} + \eta_{ri}$). Finally, the ailerons δ_{la} and δ_{ra} were employed in both symmetric and antisymmetric motions, with the purpose of correcting the shape of the aircraft. Then the input vector can be rewritten as:

$$\mathbf{u}_{SAS} = [\delta_{ele\ sym} \ \delta_{ele\ asym} \ \delta_{ail\ sym} \ \delta_{ail\ asym} \ \delta_{th} \ \delta_{rd}]^T \quad (39)$$

where $\mathbf{u}_{SAS} \in \mathbb{R}^{6 \times 1}$. The previous assumptions are mathematically represented by the following output matrix restructuring for disturbances around equilibrium:

$$\mathbf{B}_\delta = [\mathbf{B}_1 + \mathbf{B}_2 \ : \ \mathbf{B}_4 - \mathbf{B}_3 \ : \ \mathbf{B}_6 + \mathbf{B}_5 \ : \ \mathbf{B}_6 - \mathbf{B}_5 \ : \ \mathbf{B}_7 + \mathbf{B}_8 + \mathbf{B}_9 + \mathbf{B}_{10} + \mathbf{B}_{11} \ : \ (\mathbf{B}_{10} + \mathbf{B}_{11}) - (\mathbf{B}_7 + \mathbf{B}_8)] \quad (40)$$

where \mathbf{B}_j represents the j -th column of the matrix \mathbf{B} , $\mathbf{B}_\delta \in \mathbb{R}^{n \times 6}$.

The output $\mathbf{y}_{SAS} \in \mathbb{R}^{8 \times 1}$ comprises model outputs such as attitudes and angular velocities, at different points of the wing and close to the aircraft center of gravity (CG). All outputs used are measurements made by the aircraft sensors and available in the flight control system:

$$\mathbf{y}_{SAS} = [\theta_c \ \phi_c \ p_c \ r_c \ (p_r + p_l - 2p_c) \ (p_r - p_l) \ (r_r + r_l - 2r_c) \ (r_r - r_l)] \quad (41)$$

The rationale for selecting outputs in Eq. 41 is as follows: θ_c is considered to measure the SP and phugoid mode effects; ϕ_c , p_c , and r_c are selected to measure the lateral-directional motion. The 5th element of \mathbf{y}_{SAS} corresponds to a combination of signals to capture the anti-symmetric bending modes, whereas the 6th element captures the symmetric bending motion. Lastly, similarly, the signal combinations 7th and 8th capture the symmetric and anti-symmetric in-plane modes, respectively.

3.2. Model Reduction

The high order of the ITA X-HALE model is a challenge to most control techniques; therefore, a state-space reduced-order model is appropriate. For this purpose, a residualization technique [31,37] is applied to all the aerodynamic lag states and the modes with frequency above 8 Hz of the nominal model. The resulting reduced linear model (\mathbf{A}_r , \mathbf{B}_r , \mathbf{C}_r , \mathbf{D}_r) comprises nine rigid-body states of the full model (discarding ignorable variables x , y and ψ), as well as the fourteen elastic modes below 8 Hz:

$$\mathbf{x}_r = [V \ \alpha \ q \ \theta \ H \ \beta \ \phi \ p \ r \ \boldsymbol{\eta}_r^T \ \dot{\boldsymbol{\eta}}_r^T]^T \quad (42)$$

The maximum and minimum singular values of the multiple-input, multiple-output (MIMO) transfer function matrix from \mathbf{u}_{SAS} to \mathbf{y}_{SAS} for both the full-order and the reduced-order models are shown in Figure 6. It is evident that the reduced model preserves essential characteristics of the full model up to 8 Hz. Additionally, in Figure 6, the response above 10 Hz is not accurately represented by the reduced model. However, a controller with adequate stability margins should be able to accommodate this discrepancy. Similar results were verified for all velocities.

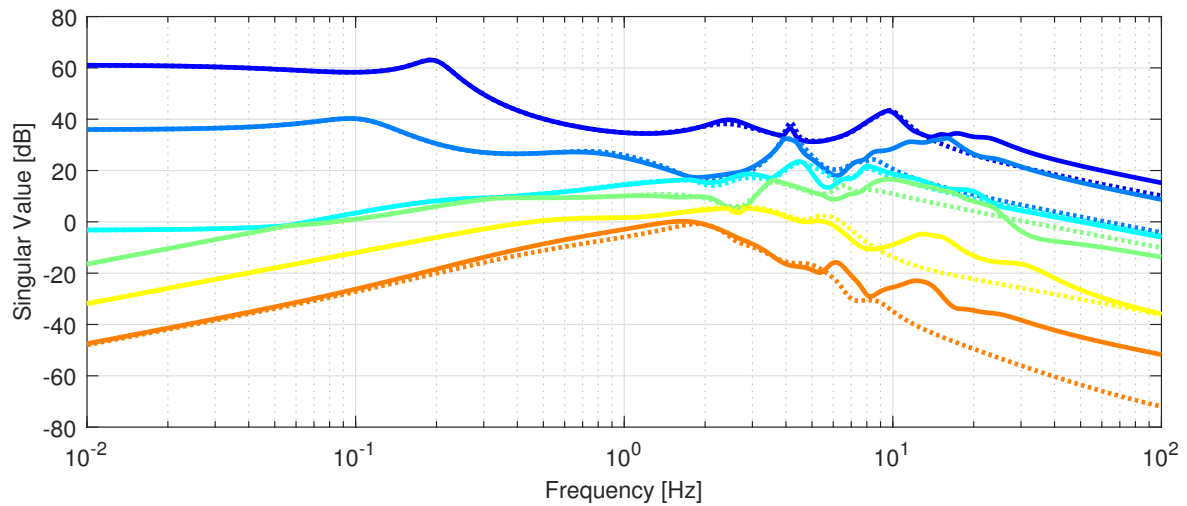


Figure 6. Comparison between the singular values of the transfer function matrices of the full- and reduced-order linear models at 16.5 m/s. The solid lines indicate the full-order model and the dashed lines the reduced-order model.

4. Numerical Results

To illustrate the proposed method, the approach detailed in Section 2 was implemented on the six-meter-span ITA X-HALE model. However, its reduced version presented in Section 3.2 was used, primarily due to computational constraints associated with model order. The control inputs from Eq. 39 and outputs from Eq. 41 were selected. For SAS design, the altitude state has been disregarded. Therefore, the linear model employed in the SAS design is represented by:

$$\dot{\mathbf{x}}_{\mathbf{r}} = \mathbf{A}_{36 \times 36} \mathbf{x}_{\mathbf{r}} + \mathbf{B}_{\delta_{36 \times 6}} \mathbf{u}_{\text{SAS}} \quad (43)$$

$$\mathbf{y}_{\text{SAS}} = \mathbf{C}_{8 \times 36} \mathbf{x}_{\mathbf{r}} \quad (44)$$

The gains were developed according to the flowchart methodology in Figure 4. The first step is to select the design points. Only velocity was selected as the scheduling variable, with intervals of 0.5 m/s, varying from 12.5 to 20.0 m/s.

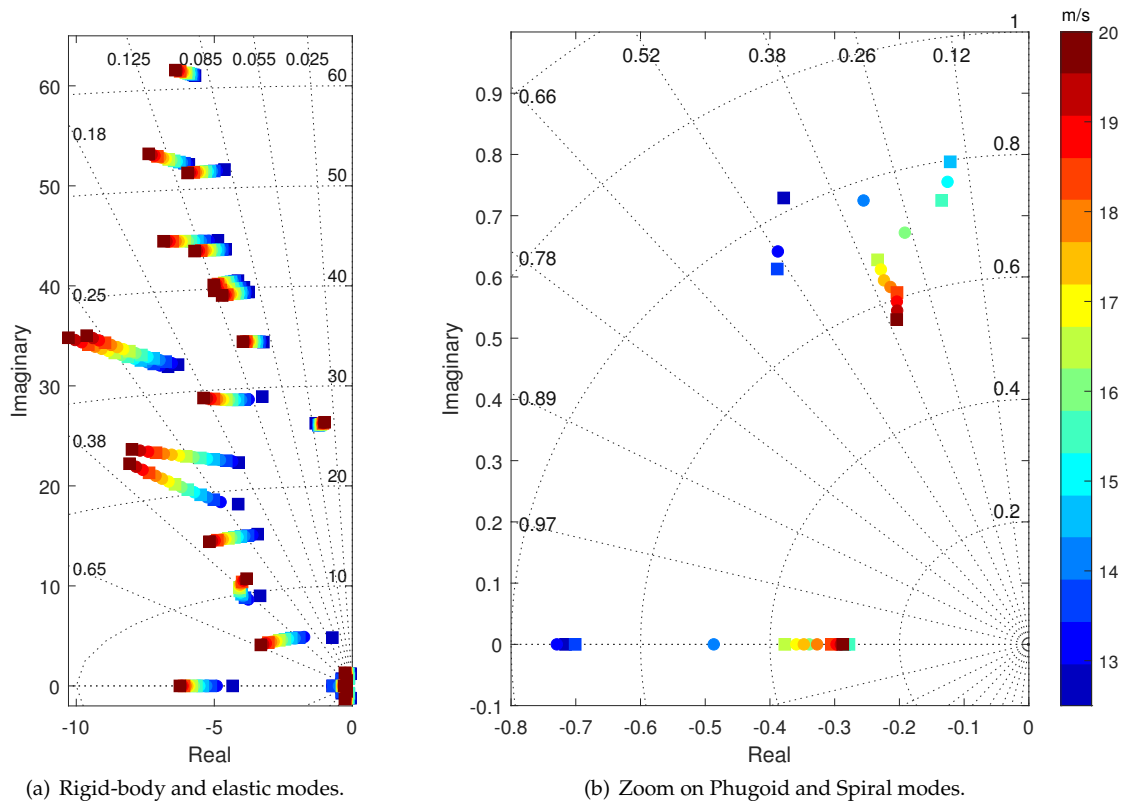


Figure 7. Pole map covering velocities ranging from 12.5 to 20.0 m/s. The squares highlight the poles corresponding to the selected velocities for the controller design.

The selection of design points was guided by the behavior of the poles. It is evident that the majority of poles exhibit satisfactory behavior concerning variations in velocity, as shown in Figure 7. However, the phugoid and spiral modes demonstrate less linear behavior, due to the nonlinearities present in the propulsive model that was based on wind-tunnel data, as presented by [Guimarães Neto et al. \[22\]](#). To obtain a reliable representation of these modes, velocities of 12.5, 13.5, 14.5, 15.5, 16.5, 18.5, and 20.0 m/s were chosen, consistent with those depicted in the membership functions of Figure 3. Other methods for selecting design points, such as the one proposed by [Al-Jiboory et al. \[38\]](#), exist but are not within the scope of analysis for this study.

Once the design points have been selected, the next step is to optimize the LQR PI. The minimization was accomplished numerically by a local search algorithm based on the Nelder-Mead simplex method [39]. A good compromise between closed-loop response and demanded actuation energy was obtained for the following choice of weighting matrices:

$$Q = \begin{bmatrix} \mathbf{I}_{7 \times 7} & \mathbf{0}_{7 \times 1} & \mathbf{0}_{7 \times 14} & \mathbf{0}_{7 \times 14} \\ \mathbf{0}_{1 \times 7} & 0.75 & \mathbf{0}_{1 \times 14} & \mathbf{0}_{1 \times 14} \\ \mathbf{0}_{14 \times 7} & \mathbf{0}_{14 \times 1} & \left(\frac{1}{(i_1^{14})^2} \right) \mathbf{I}_{14 \times 14} & \mathbf{0}_{14 \times 14} \\ \mathbf{0}_{14 \times 7} & \mathbf{0}_{14 \times 1} & \mathbf{0}_{14 \times 14} & \left(\frac{1}{(i_1^{14})^2} \right) \mathbf{I}_{14 \times 14} \end{bmatrix} \quad (45)$$

$$\mathbf{R} = \text{diag} \left(\frac{1}{15^2}, \frac{1}{15^2}, \frac{1}{15^2}, \frac{1}{15^2}, \frac{1}{0.02^2}, \frac{1}{0.1^2} \right) \quad (46)$$

The Q matrix was chosen as an identity matrix for the rigid body states, with a reduction in weighting for r . The elastic modes were weighted to exert a more significant influence on the lower frequency modes and a lesser impact on the higher frequency modes. This was achieved using the

weight $\frac{1}{(i!)^2}$, where i ranges from 1 to 14, corresponding to the number of elastic states. Regarding the R matrix, Bryson's rule was applied, assigning a higher weight to the rudder.

Finally, the last step involves applying the LMI presented in Eq. 33, which arises from the fuzzy system described in Section 2.2.2. The state-space system considered for the LMI is the closed-loop system with gains determined by the LQR PI minimization for each design point. The design variable κ is further analyzed in the next section.

4.1. κ Stability Analysis

The new design variable κ is incorporated into the second step outlined in Section 2.5. To assess its impact on stability enhancement, a range of κ values, spanning from 10^5 to 10^{-10} , was systematically applied to the LMI set.

Following the application of LMI on top of the LQR design, the disk margin performance between LQR and LMI for different values of κ is compared, calculated according to Lavretsky and Wise [40]. As illustrated in Figure 8, the LQR design leads to instability at 13.5 m/s, exhibiting an overall poor margin with the entire range below 4.5 dB. Conversely, the methodology proposed for gain design reveals that higher values of κ fail to stabilize the entire range, and with the highest value, the margins are even worse than the pure LQR design. However, as the value of κ decreases, stability margins substantially increase, with the best result achieved when κ is equal to 10^{-3} . Examining the sum of the Root Mean Square (RMS) values of the approximation described in Eq. 31, presented in Figure 9, it is evident that for this value, the approximation converges close to zero and achieves an almost steady value for smaller κ values. All solutions where the RMS value was smaller than 1 achieved good stability margins, indicating that once the approximation is sufficiently accurate, stability margins increase and the global stability is assured. However, it is essential to note that this κ value is problem-specific.

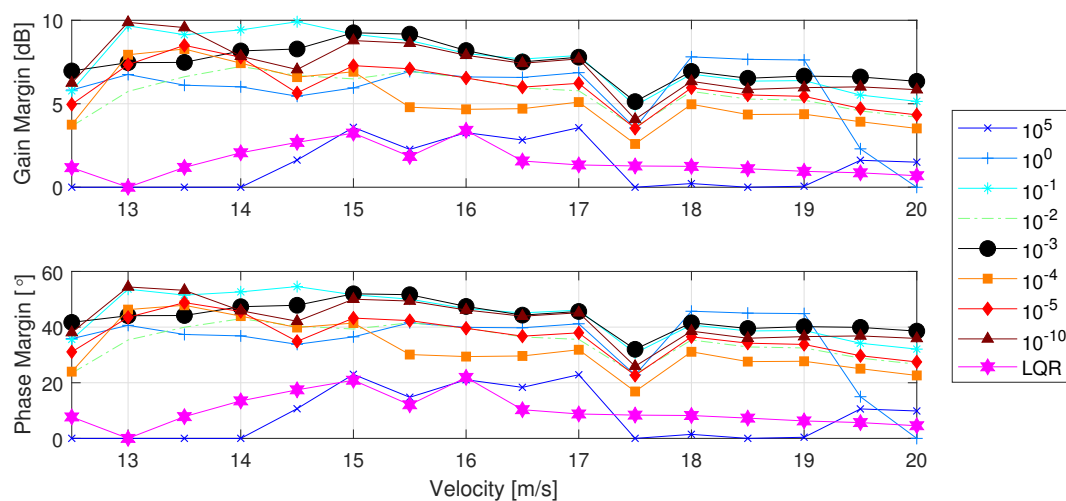


Figure 8. Stability margins for closed loop system for ITA X-HALE model, comparison between LQR and LMI design.

4.2. Nonlinear Simulations

After the stability study, simulations focusing on performance degradation analysis at different points used in the design were evaluated. These nonlinear simulations also aim to show the system performance improvement at intermediate velocities where the LMI described in Eq. 33 is considered in the controller design.

The simulations were performed with three different control configurations: open loop, closed loop considering the gain calculated through LQR only, and gains calculated using the methodology outlined in the flowchart 4, which combines LQR and LMI with $\kappa = 10^{-3}$, referred to simply as FGS.

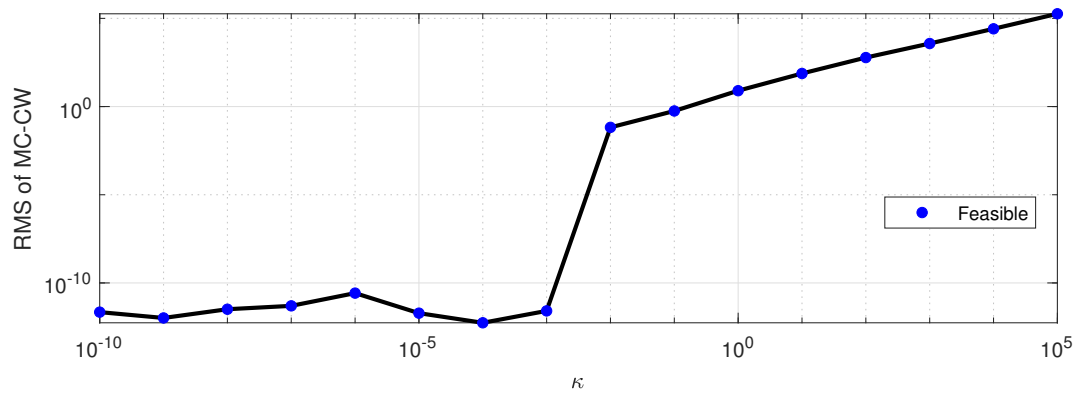


Figure 9. RMS values of the approximation $\mathbf{M}(\omega)\mathbf{C}(\omega) - \mathbf{C}(\omega)\mathbf{W} = 0$ for different values of κ .

Table 1. The RMS values of rigid body outputs during straight flight at a velocity of 17.0 m/s, under the influence of vertical and horizontal wind gusts, are presented for two distinct output feedback realizations and open loop.

	Open Loop	LQR	FGS
V_c [m/s]	0.193	0.403	0.434
H [m]	0.365	2.99	1.280
θ_c [°]	1.54	1.98	1.34
q_c [°/s]	4.61	5.25	3.63
β [°]	4.01	2.10	3.21
r_c [°/s]	1.22	0.68	0.26
ϕ_c [°]	6.93	3.26	5.65
p_c [°/s]	9.64	6.07	7.13

Table 2. The RMS values of control inputs during straight flight at a velocity of 17.0 m/s, under the influence of vertical and horizontal wind gusts, are presented for two distinct output feedback realizations and open loop.

	Open Loop	LQR	FGS
δ_{ra} [°]	0.000	4.720	0.869
δ_{la} [°]	0.000	1.630	0.493
δ_{lo} and δ_{ro} [°]	0.000	1.170	0.152
δ_{li} and δ_{ri} [°]	0.000	0.850	0.186
η_{lo} and η_{li} [-]	0.000	0.136	0.105
η_{ro} and η_{ri} [-]	0.000	0.125	0.102
η_c [-]	0.000	0.128	0.103

Table 3. The RMS values of wingtip outputs during straight flight at a velocity of 17.0 m/s, under the influence of vertical and horizontal wind gusts, are presented for two distinct output feedback realizations and open loop.

	Open Loop	LQR	FGS
T_{zl} [m]	0.023	0.157	0.022
T_{zr} [m]	0.033	0.206	0.025
p_{lwt} [°/s]	10.00	10.40	7.23
p_{rwt} [°/s]	9.26	10.50	6.80
r_{lwt} [°/s]	1.25	0.90	0.35
r_{rwt} [°/s]	1.30	1.41	0.53
η_{zlwt} [g]	0.168	0.194	0.171
η_{zrwt} [g]	0.174	0.172	0.140

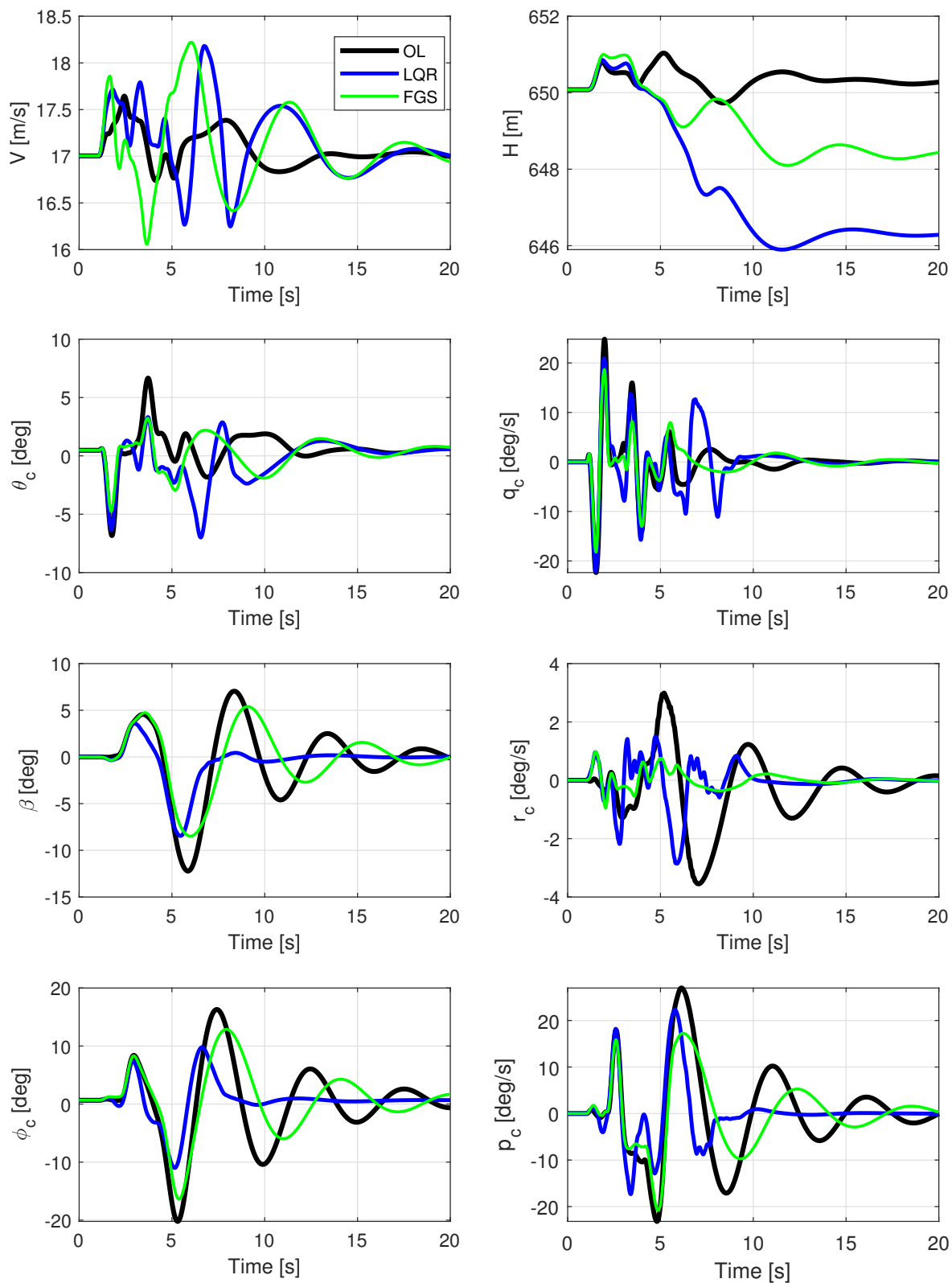


Figure 10. Rigid body outputs for a velocity of 17.0 m/s, subjected to vertical and horizontal wind gusts, with two different output feedback realizations and open loop.

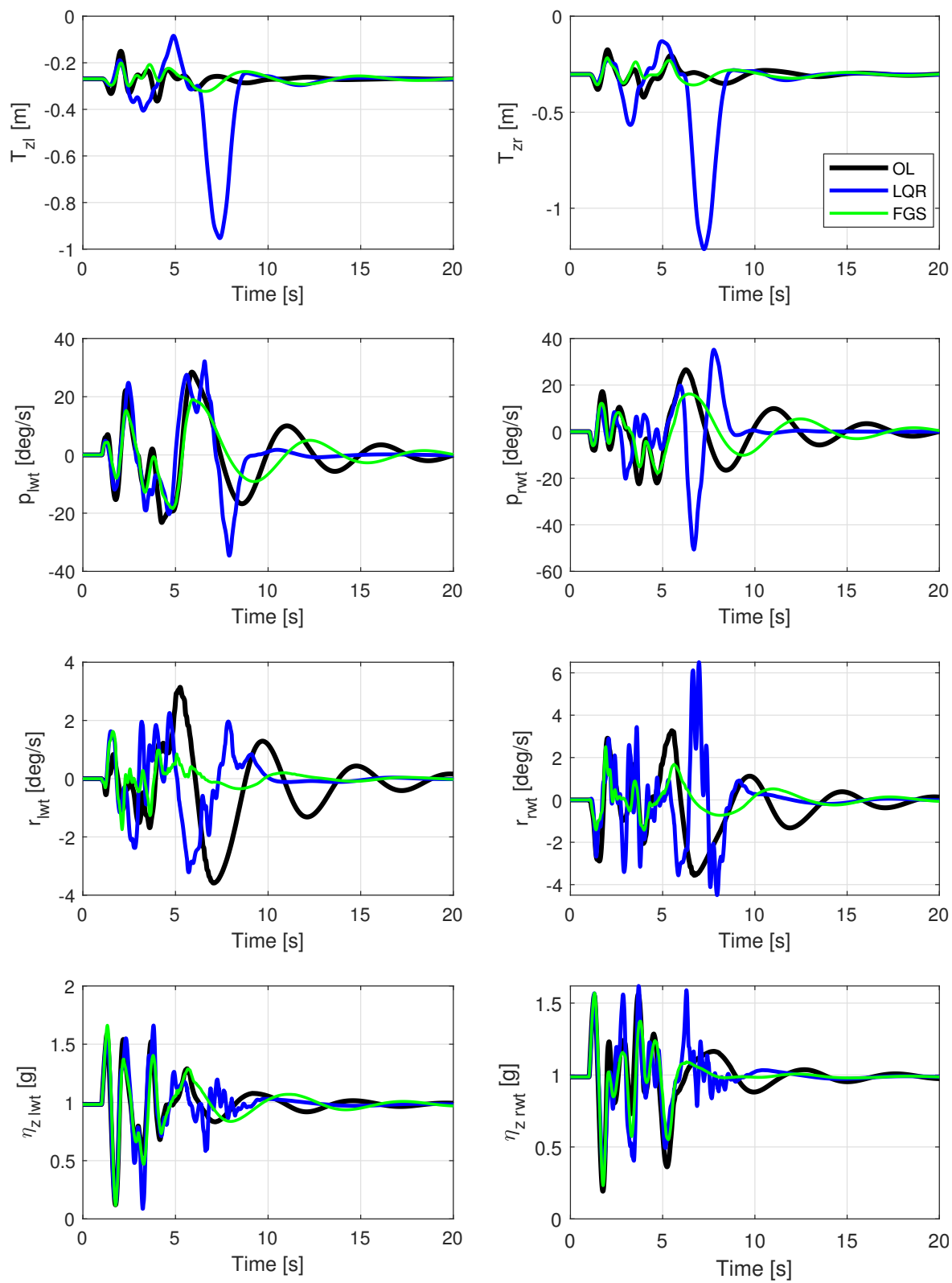


Figure 11. Wingtip outputs for a velocity of 17.0 m/s, subjected to vertical and horizontal wind gusts, with two different output feedback realizations and open loop.

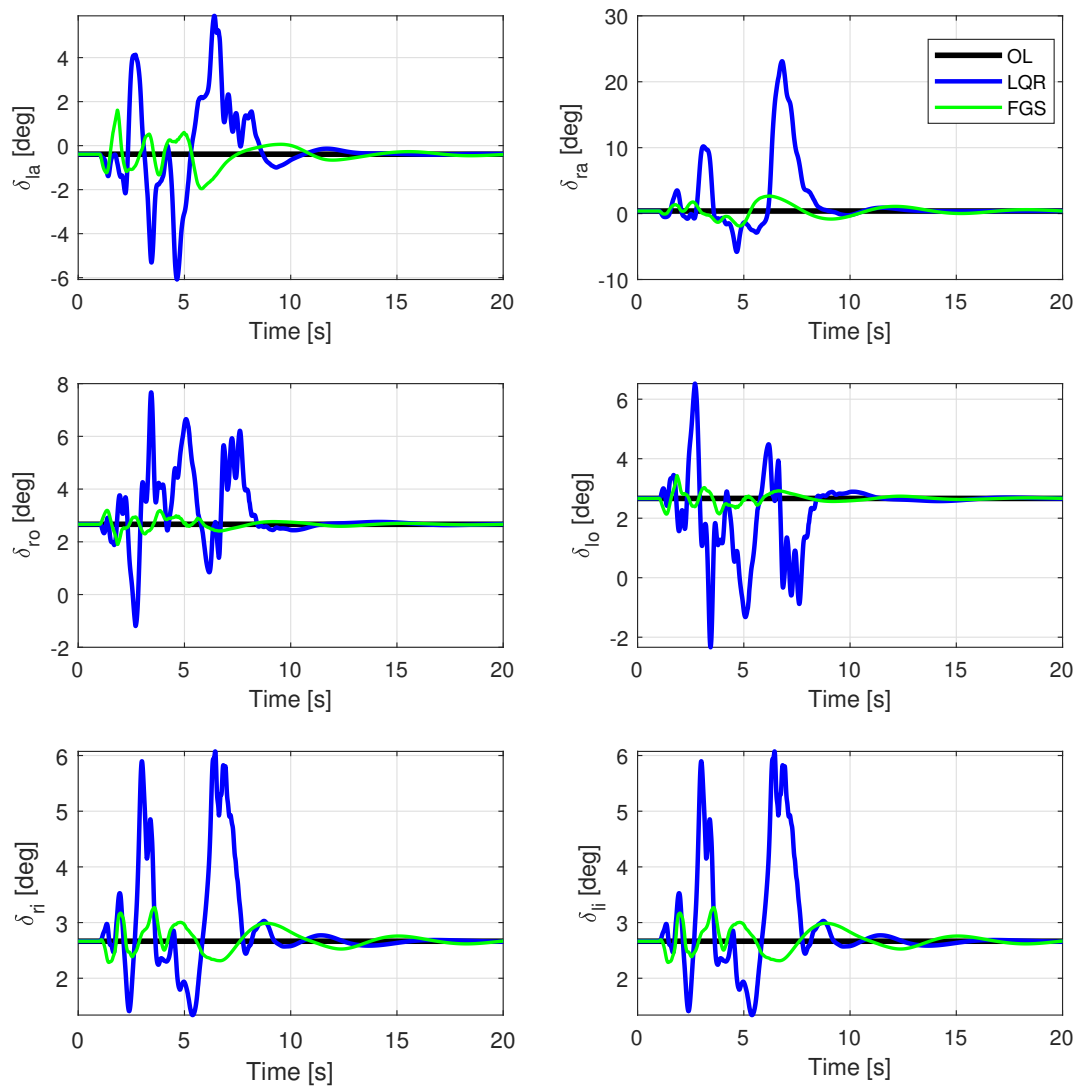


Figure 12. Control surfaces for a velocity of 17.0 m/s, subjected to vertical and horizontal wind gusts, with two different output feedback realizations and open loop.

To assess a scenario where the system experiences disturbance around an equilibrium point, simulations were conducted with vertical and horizontal gusts featuring a one-minus-cosine profile during straight-level flight at 17.0 m/s. Figs. 10 to 13 illustrate the results of a simulation in which the aircraft is perturbed by two lateral and two vertical gusts. These gusts have a maximum amplitude of 3 m/s and are fixed in space, with vertical gusts occurring from 17 to 34 m and 51 to 68 m, and horizontal gusts from 34 to 51 m and 68 to 95 m.

Figure 10 presents rigid body outputs. Gains calculated using only LQR demonstrate commendable performance, particularly in the context of lateral-directional motion, exhibiting high attenuation for both β and ϕ_c . The controller that combines both techniques exhibits the best results for longitudinal motion, displaying smaller variations in θ_c and q_c . This superior performance is further evident in the RMS values in Table 1. However, velocity and altitude have deteriorated due to the increased control energy used in all motors, as indicated by the RMS values in Table 2.

Now, examining the wingtip outputs in Figure 11, it is evident that the gain calculated by the LMI was able to yield the smallest wingtip displacement (T_z), consequently resulting in the lowest RMS value, as shown in Table 3. The results for r_{wt} , both left and right, exhibit the most significant attenuation in the FGS design and are associated with wing in-plane motion. Conversely, the LQR-only design resulted in substantial wing displacements and, notably, the poorest outcome for the rates.

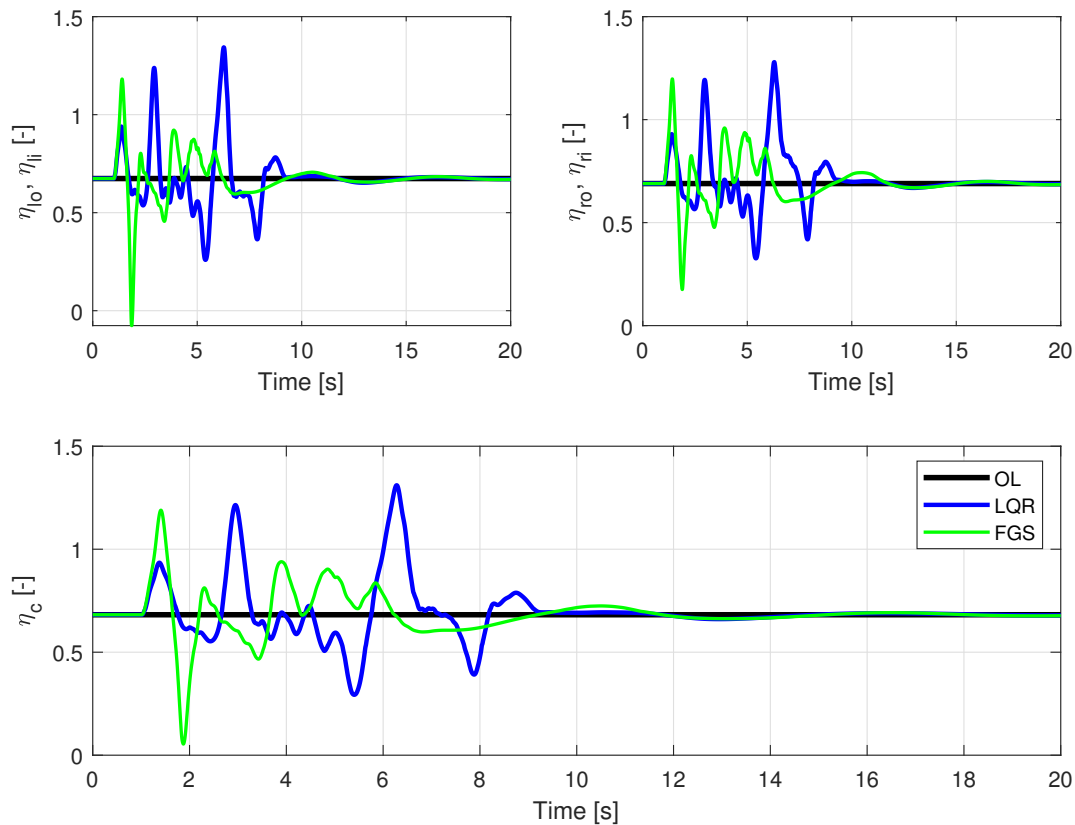


Figure 13. Motor entries for a velocity of 17.0 m/s, subjected to vertical and horizontal wind gusts, with two different output feedback realizations and open loop.

Concerning control energy, as depicted in Figure 12 and Figure 13, and highlighted in Table 2, the gains calculated with FGS exhibited superior performance, utilizing less control effort compared to the LQR. This is evident for both control surfaces and motors. Table 2 illustrates the RMS values. Although the physical limits were exceeded by the motors, the FGS design performed better in this regard.

Finally, the controller's performance was analyzed when the aircraft was exposed to a von Kármán wind turbulence as an external disturbance. Results in the same manner as the results shown above are presented in Figs. 14 to 17.

Table 4. The RMS values of rigid body outputs during straight flight at a velocity of 14.5 m/s, under the influence of a von Kármán wind turbulence, are presented for two distinct output feedback realizations and open loop.

	Open Loop	LQR	FGS
V_c [m/s]	0.812	0.917	0.577
H [m]	4.04	4.80	5.10
θ_c [°]	4.04	3.84	1.93
q_c [°/s]	6.89	9.44	4.53
β [°]	5.78	2.89	4.51
r_c [°/s]	1.33	1.21	0.27
ϕ_c [°]	7.72	2.06	5.64
p_c [°/s]	9.66	3.50	6.59

Table 5. The RMS values of wingtip outputs during straight flight at a velocity of 14.5 m/s, under the influence of a von Kármán wind turbulence, are presented for two distinct output feedback realizations and open loop.

	Open Loop	LQR	FGS
T_{zl} [m]	0.041	0.138	0.034
T_{zr} [m]	0.047	0.142	0.039
p_{lwt} [°/s]	10.20	8.86	6.98
p_{rwt} [°/s]	10.20	9.22	6.78
r_{lwt} [°/s]	1.66	1.78	0.82
r_{rwt} [°/s]	1.85	2.42	0.84
η_{zlwt} [g]	0.284	0.424	0.263
η_{zrwt} [g]	0.206	0.365	0.164

Table 6. The RMS values of control inputs during straight flight at a velocity of 14.5 m/s, under the influence of a von Kármán wind turbulence, are presented for two distinct output feedback realizations and open loop.

	Open Loop	LQR	FGS
δ_{ra} [°]	0.000	4.990	0.696
δ_{la} [°]	0.000	4.800	0.520
δ_{lo} and δ_{ro} [°]	0.000	3.530	0.293
δ_{li} and δ_{ri} [°]	0.000	1.910	0.262
η_{lo} and η_{li} [-]	0.000	0.204	0.096
η_{ro} and η_{ri} [-]	0.000	0.191	0.098
η_c [-]	0.000	0.196	0.097

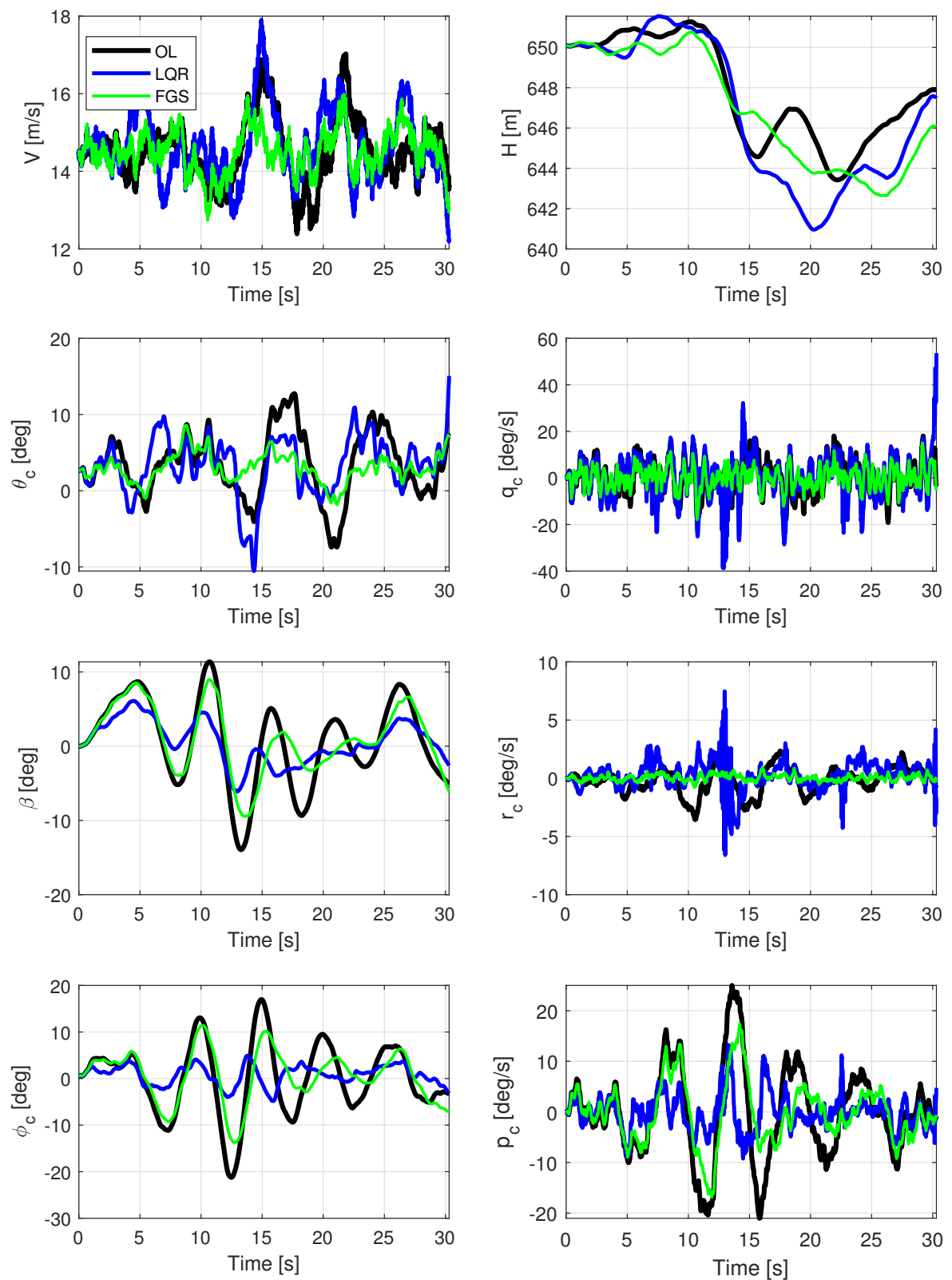


Figure 14. Rigid body outputs for a velocity of 14.5 m/s, subjected to von Kármán wind turbulence, with two different output feedback realizations and open loop.

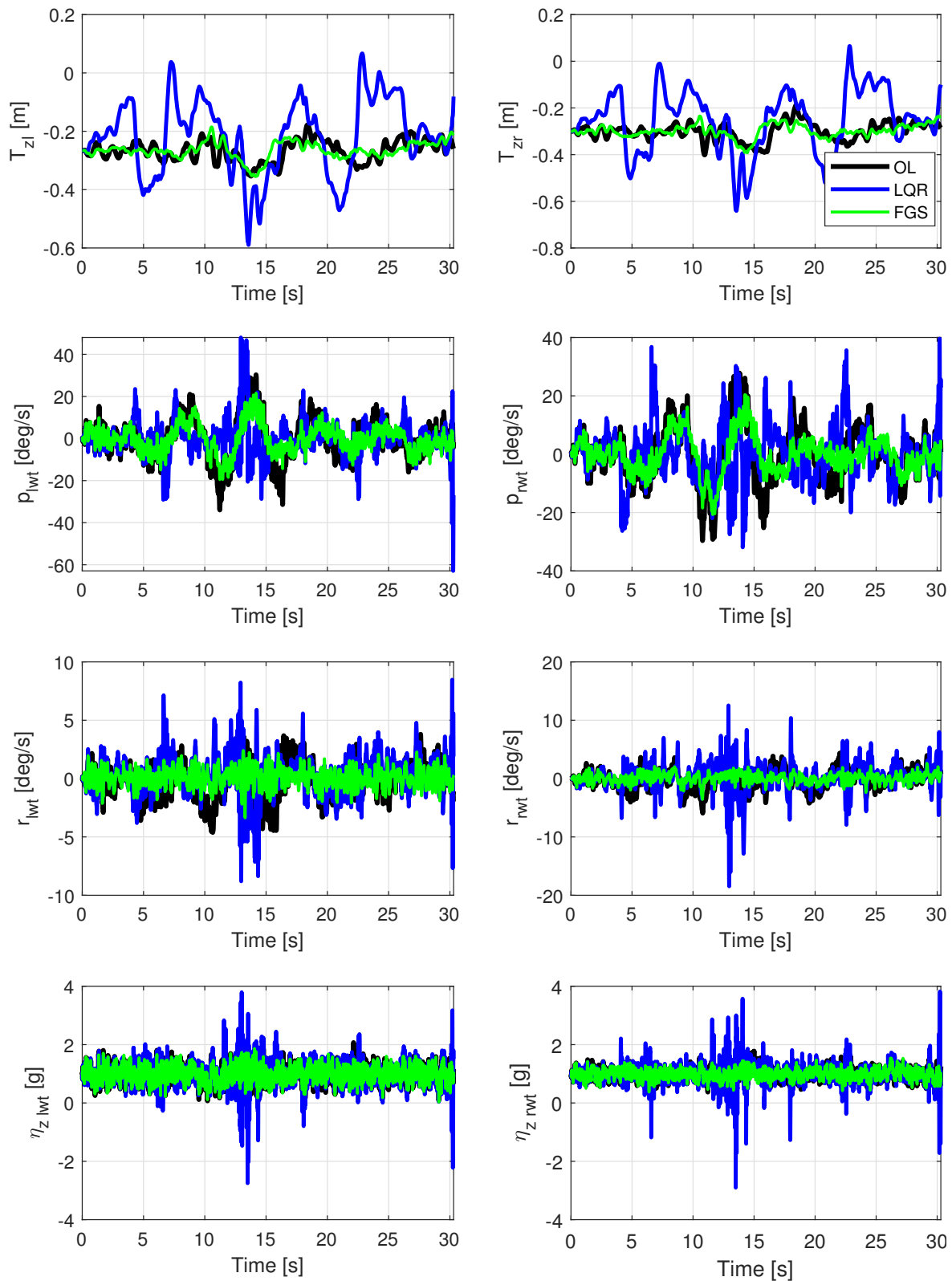


Figure 15. Wingtip outputs for a velocity of 14.5 m/s, subjected to von Kármán wind turbulence, with two different output feedback realizations and open loop.

The rigid body results in Figure 14 exhibit a similar pattern in terms of attenuations, with the LQR showing a superior response in lateral-directional motion and the FGS outperforming in longitudinal motion. Notably, instabilities are observed in q_c for the LQR design, particularly as the phugoid mode is degenerate and couples with the spiral mode, leading to instability at a flight velocity of 13.0 m/s. Consequently, whenever the aircraft traverses this unstable region, the LQR design exhibits an

inappropriate response, causing the simulation to crash after 30 s. In the other two instances when the aircraft passes through the unstable region, the aircraft recovers because the turbulence itself increases the aircraft's velocity.

Examining both Figure 14 and Table 4, it is evident that the highest attenuation was achieved by the controller designed with LQR for lateral motion. However, the FGS design can ensure stability at intermediary points while still offering some improvement over the open-loop response.

The wingtip outputs depicted in Figure 15 reveal a greater attenuation in wingtip displacement for the controller that combines LQR and LMI methods compared to the LQR-only controller. This is attributed to the more pronounced aileron deflections for the LQR design, as observed in Figure 16, resulting in a greater aerodynamic force on the ailerons and, consequently, in wingtip displacement. While Figure 15 may not clearly indicate whether the FGS controller outperforms the open-loop one, Table 5 demonstrates that the FGS controller exhibited better performance for all outputs.

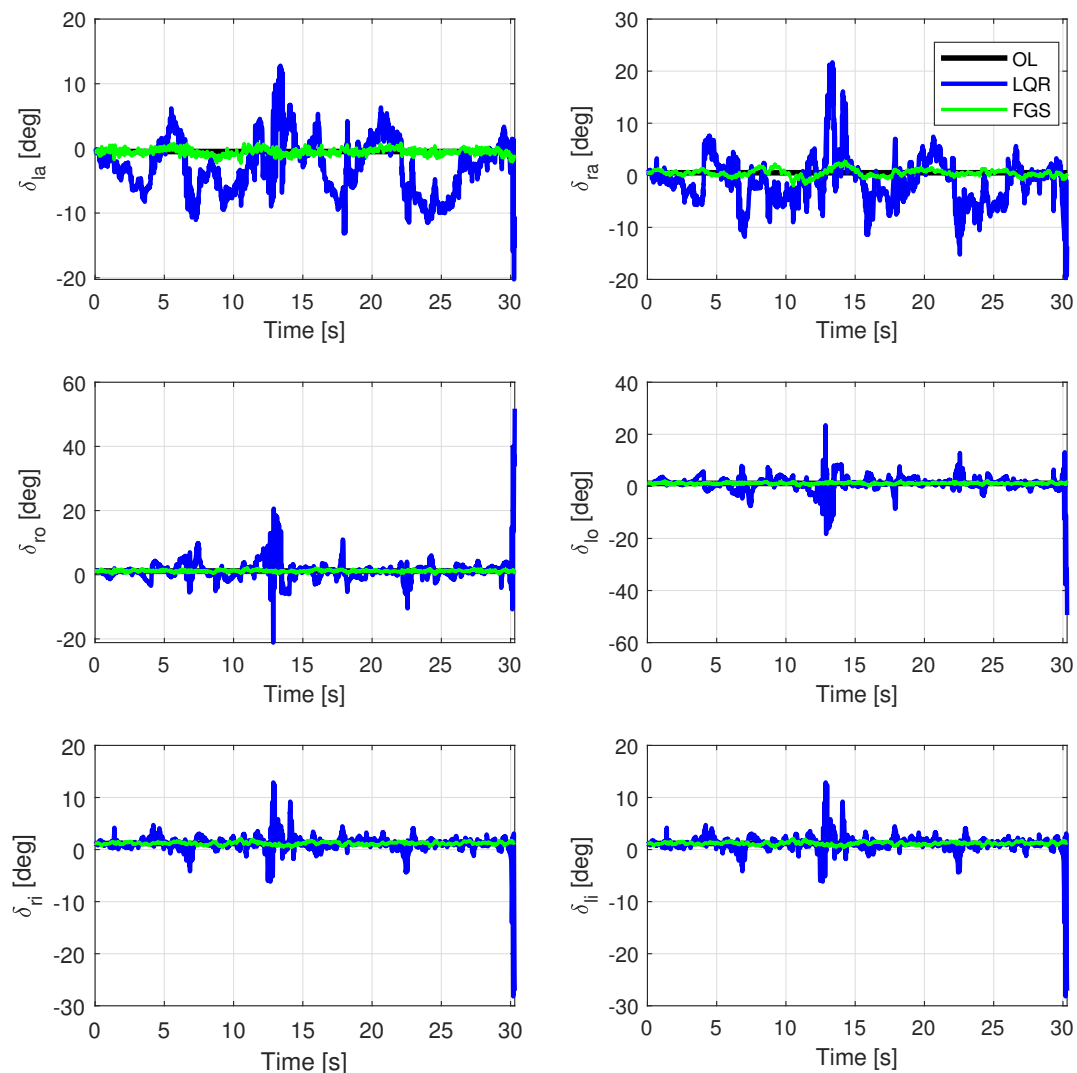


Figure 16. Control surfaces for a velocity of 14.5 m/s, subjected to von Kármán wind turbulence, with two different output feedback realizations and open loop.

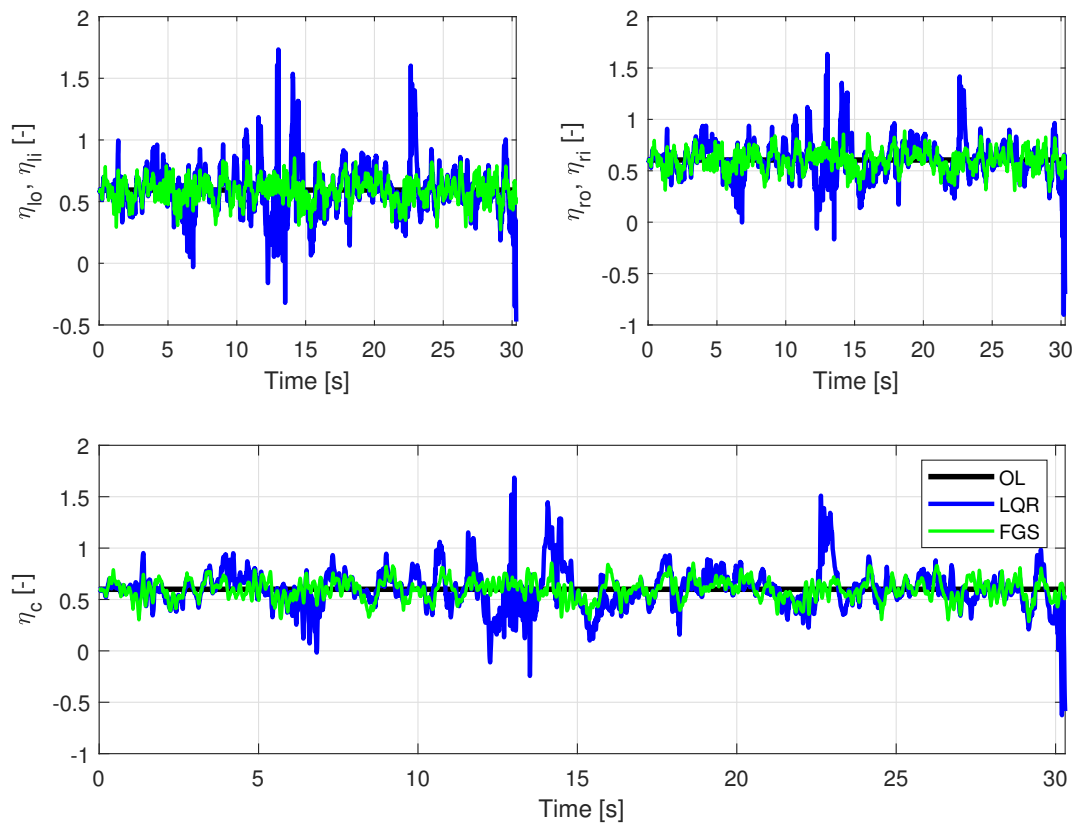


Figure 17. Motor entries for a velocity of 14.5 m/s, subjected to von Kármán wind turbulence, with two different output feedback realizations and open loop.

The FGS design demonstrated lower expended control energy, consistent with the previous simulation. In terms of motor usage, as shown in Figure 17, the FGS was able to stay within the limits, while the LQR exceeded the limits on several occasions. This is particularly crucial for HALE aircraft, where control of energy usage is critical. The results presented in Table 6 underscore a significant improvement in this regard.

5. Conclusion

An output feedback gain-scheduling approach based on fuzzy logic has been proposed in this paper to solve stability issues in intermediate regions to those chosen for the linear controller design. The approach combines closed-loop performance improvement via LQR and stability enforcement in the whole flight envelope through the Lyapunov direct method. The proposed approximation for the output feedback demonstrates effectiveness. As κ decreases, the approximation tends toward zero, ensuring overall stability.

Results comparing the proposed approach with traditional interpolation-based gain-scheduling techniques showed that the present technique had overall better performance, smoother closed-loop responses, and higher and more constant gain and phase margins in the entire velocity envelope. Thus, there is an enormous potential of reducing the time necessary in the control law development without the need to run several simulations (e.g. Monte-Carlo simulations) to look for stability issues in the entire envelope.

In this paper, the LQR method was selected to optimize the controller for performance. Nevertheless, it is worth noting that other techniques can be employed in this step of the process.

Funding: This study was financed in part by the Coordenação de Aperfeiçoamento de Pessoal de Nível Superior - Brasil (CAPES) - Finance Code 001. Also the authors would like to thank the financial support from Finep and Embraer S.A. under grant number 01.14.0185.00.

Acknowledgments: The authors would like to express my deepest gratitude to Dr. Antônio Bernardo Guimarães Neto for generously providing all models used in this work, offering expert guidance in troubleshooting and refining algorithmic implementations, and contributing insightful design suggestions and rigorous manuscript revisions. Without Dr. Guimarães Neto's dedicated support and intellectual collaboration, this research would not have been possible. They also gratefully acknowledge Dr. Rafael Mendes Bertolin for his invaluable assistance in the design process, which helped resolve technical queries and propose innovative solutions that greatly enhanced the project's development and refinement. The dedicated support and intellectual collaboration of both researchers were instrumental to the successful completion of this study.

Conflicts of Interest: The authors declare no conflicts of interest.

Abbreviations

The following abbreviations are used in this manuscript:

CG	Center of Gravity
FGS	Fuzzy Gain-Scheduling
HALE	High Altitude Long Endurance
LMI	Linear Matrix Inequalities
LQR	Linear Quadratic Regulator
MIMO	Multiple-Input, Multiple-Output
OL	Open Loop
PI	Performance Index
RMS	Root Mean Square
SAS	Stability Augmentation System
SP	Short-Period
TS	Takagi-Sugeno

References

- Schmidt, D.K. *Modern Flight Dynamics*, 1 st ed.; McGraw-Hill: New York, 2012. ISBN: 978-0-07-339811-2.
- Cesnik, C.E.S.; Senatore, P.J.; Su, W.; Atkins, E.M.; Shearer, C.M. X-HALE: A very flexible unmanned aerial vehicle for nonlinear aeroelastic tests. *AIAA journal* **2012**, *50*, 2820–2833.
- Silvestre, F.J.; Neto, A.B.G.a.; Bertolin, R.M.; Silva, R.G.A.D.; Paglione, P. Aircraft Control Based on Flexible Aircraft Dynamics. *Journal of Aircraft* **2017**, *54*, 262–271.
- Guimarães Neto, A.B.; Silva, R.G.; Paglione, P.; Silvestre, F.J. Formulation of the Flight Dynamics of Flexible Aircraft Using General Body Axes. *AIAA Journal* **2016**, pp. 3516–3534.
- Fan, W.; Liu, H.H.T.; Kwong, R.H.S. Gain-Scheduling Control of Flexible Aircraft with Actuator Saturation and Stuck Faults. *Journal of Guidance, Control, and Dynamics* **2017**.
- Bertolin, R.M.; Guimarães Neto, A.B.; Barbosa, G.C.; Paulino, J.A.; Silvestre, F.J. Design of Stability Augmentation Systems for Flexible Aircraft Using Projective Control. *Journal of Guidance, Control, and Dynamics* **2021**, *44*, 2244–2262, [<https://doi.org/10.2514/1.G005783>]. <https://doi.org/10.2514/1.G005783>.
- Barbosa, G.C.; Bertolin, R.M.; Paulino, J.A.; Guimarães Neto, A.B.; Silvestre, F.J. Design and Flight Test of a Stability Augmentation System for a Flexible Aircraft. *Journal of Guidance, Control, and Dynamics* **2022**, *45*, 1709–1723, [<https://doi.org/10.2514/1.G006271>]. <https://doi.org/10.2514/1.G006271>.
- Alazard, D. Robust H Design for Lateral Flight Control of Highly Flexible Aircraft. *Journal of Guidance, Control, and Dynamics* **2002**, *25*, 502–509.
- Cesnik, C.E.S.; Su, W. Nonlinear aeroelastic simulation of X-HALE: a very flexible UAV. In Proceedings of the 49th AIAA Aerospace Sciences Meeting including the New Horizons Forum and Aerospace Exposition, Orlando, FL, 2011.
- Cook, R.G.; Palacios, R.; Goulart, P. Robust Gust Alleviation and Stabilization of Very Flexible Aircraft. *AIAA Journal* **2013**, *51*, 330–340.
- Qu, Z.; Annaswamy, A.M.; Lavretsky, E. Adaptive output-feedback control for a class of multi-input-multi-output plants with applications to very flexible aircraft. *2016 American Control Conference (ACC)* **2016**.
- Qu, Z.; Annaswamy, A.M. Adaptive Output-Feedback Control with Closed-Loop Reference Models for Very Flexible Aircraft. *Journal of Guidance, Control, and Dynamics* **2016**, *39*, 873–888.

13. Hjartarson, A.; Seiler, P.; Balas, G.J. LPV analysis of a gain scheduled control for an aeroelastic aircraft. *Proceedings of the American Control Conference* **2014**, pp. 3778–3783. <https://doi.org/10.1109/ACC.2014.6859301>.
14. Rugh, W.J.; Shamma, J.S. Research on gain scheduling. *Automatica* **2000**, *36*, 1401–1425.
15. Barbosa, G.C.; Bertolin, R.; González, P.J.; Guimarães Neto, A.B.; Silvestre, F.J. Fuzzy Gain-Scheduling Applied for a Very Flexible Aircraft. *AIAA Guidance, Navigation, and Control Conference, AIAA SciTech Forum* **2018**.
16. Fujimori, A.; Wu, Z.; Nikiforuk, P.; Gupta, N. A design of ALFLEX flight control system using fuzzy gain-scheduling. *AIAA Guidance, Navigation, and Control Conference* **1998**, pp. 1739–1745.
17. Gonsalves, P.G.; Zacharias, G.L. Fuzzy logic gain scheduling for flight control. In Proceedings of the Proceedings of 1994 IEEE 3rd International Fuzzy Systems Conference, Orlando, FL, June 1994; pp. 952–957 vol.2. <https://doi.org/10.1109/FUZZY.1994.343863>.
18. Schram, G. Intelligent flight control: A fuzzy logic approach. PhD thesis, Delft University of Technology, 1998. Thesis of Doctor in Science in Electrical Engineering, Mathematics and Computer Science.
19. Tanaka, K.; Ikeda, T.; Wang, H.O. Robust stabilization of a class of uncertain nonlinear systems via fuzzy control: quadratic stabilizability, H^∞ control theory, and linear matrix inequalities. *IEEE Transactions on Fuzzy Systems* **1996**, *4*, 1–13. <https://doi.org/10.1109/91.481840>.
20. BARBOSA, G.C.; GUIMARÃES NETO, A.B.; BERTOLIN, R.M.; SILVESTRE, F.J. Fuzz Gain-Scheduling for MIMO Systems Applied to Flexible Aircraft Control. In Proceedings of the International Forum on Aeroelasticity and Structural Dynamics - IFASD, Savannah, 2019.
21. Jones, J.R.; Cesnik, C.E.S. Preliminary flight test correlations of the X-HALE aeroelastic experiment. *The Aeronautical Journal* **2015**, *119*, 855–870. <https://doi.org/10.1017/S0001924000010952>.
22. Guimarães Neto, A.B.; Barbosa, G.C.; Paulino, J.A.; Bertolin, R.M.; Nunes, J.S.M.; González, P.J.; Cardoso-Ribeiro, F.L.; Morales, M.A.V.; da Silva, R.G.A.; Bussamra, F.L.S.; et al. Flexible Aircraft Simulation Validation with Flight Test Data. *AIAA Journal* **2023**, *61*, 285–304, <https://doi.org/10.2514/1.J060960>. <https://doi.org/10.2514/1.J060960>.
23. Stevens, B.L.; Lewis, F.L.; Johnson, E.N. *Aircraft control and simulation: dynamics, controls design, and autonomous systems*, 3 nd ed.; John Wiley & Sons, 2015.
24. Takagi, T.; Sugeno, M. Fuzzy identification of systems and its applications to modeling and control. *IEEE Transactions on Systems, Man, and Cybernetics* **1985**, SMC-15, 116–132. <https://doi.org/10.1109/TSMC.1985.6313399>.
25. Tanaka, K.; Wang, H.O. *Fuzzy Control Systems Design and Analysis: a Matrix Inequality Approach*; John Wiley & Sons: New York, NY, 2001.
26. LYAPUNOV, A.M. The general problem of the stability of motion. *International Journal of Control* **1992**, *55*, 531–534.
27. Crusius, C.A.; Trofino, A. Sufficient LMI conditions for output feedback control problems. *IEEE Transactions on Automatic Control* **1999**, *44*, 1053–1057.
28. Golub, G.H.; Van, C.F. *Matrix computations*; Johns Hopkins University Press: Baltimore, MD, 1996; p. 170.
29. Mozelli, L.A.; Campos, C.D.; Palhares, R.M.; Tôrres, L.A.B.; Mendes, E.M.A.M. Chaotic synchronization and information transmission experiments: a fuzzy relaxed H_∞ control approach. *Circuits, Systems, and Signal Processing* **2007**, *26*, 427–449.
30. Nguyen, A.T.; Márquez, R.; Guerra, T.M.; Dequidt, A. Improved LMI Conditions for Local Quadratic Stabilization of Constrained Takagi-Sugeno Fuzzy Systems. *International Journal of Fuzzy Systems* **2017**, *19*, 225–237.
31. Guimarães Neto, A.B. Flight dynamics of flexible aircraft using general body axes: a theoretical and computational study. PhD thesis, Instituto Tecnológico de Aeronáutica, São José dos Campos, 2014. Thesis of Doctor in Science in Flight Mechanics.
32. Guimarães Neto, A.B.; Silva, R.G.; Paglione, P.; Silvestre, F.J. Formulation of the Flight Dynamics of Flexible Aircraft Using General Body Axes. *AIAA J.* **2016**, *54*, 3516–3534.
33. Albano, E.; Rodden, W.P. A doublet-lattice method for calculating lift distributions on oscillating surfaces in subsonic flows. *AIAA Journal* **1969**, *7*, 279–285. <https://doi.org/10.2514/3.5086>.
34. Hedman, S.G. Vortex lattice method for calculation of quasi steady state loadings on thin elastic wings. Technical Report 105, Aeronautical Research Institute of Sweden, Stockholm, 1965.
35. Eversman, W.; Tewari, A. Consistent rational function approximation for unsteady aerodynamics. *Journal of Aircraft* **1991**, *29*, 545–552. <https://doi.org/10.2514/3.46062>.

36. Kálmán, T.P.; Giesing, J.P.; Rodden, W.P. Spanwise distribution of induced drag in subsonic flow by the vortex lattice method. *Journal of Aircraft* **1970**, *7*, 574–576. <https://doi.org/10.2514/3.44219>.
37. Skogestad, S.; Postlethwaite, I. *Multivariable feedback control: Analysis and Design*; John Wiley: Hoboken, US-NJ, 2005.
38. Al-Jiboory, A.K.; Zhu, G.; Swei, S.S.M.; Su, W.; Nguyen, N.T. LPV modeling of a flexible wing aircraft using modal alignment and adaptive gridding methods. *Aerospace Science and Technology* **2017**, *66*, 92–102. <https://doi.org/https://doi.org/10.1016/j.ast.2017.03.009>.
39. Lagarias, J.; Reeds, J.; Wright, M.; Wright, P. Convergence Properties of the Nelder-Mead Simplex Method in Low Dimensions. *SIAM Journal on Optimization* **1998**, *9*, 112–147, [<https://doi.org/10.1137/S1052623496303470>]. <https://doi.org/10.1137/S1052623496303470>.
40. Lavretsky, E.; Wise, K. Robust and adaptive control: With aerospace applications, ser. *Advanced textbooks in control and signal processing*. London and New York: Springer **2013**.

Disclaimer/Publisher’s Note: The statements, opinions and data contained in all publications are solely those of the individual author(s) and contributor(s) and not of MDPI and/or the editor(s). MDPI and/or the editor(s) disclaim responsibility for any injury to people or property resulting from any ideas, methods, instructions or products referred to in the content.